RESEARCH PAPER

IPSCs reprogrammed from senescent granulosa cells with age for generating germ cells

Dai Heng[1,2,3#], Kairang Jin[1,2#], Guoxing Yin[1,2], Chenglei Tian[1,2,4], Xiaoyan Sheng[5], Jiangtao Lu[1,2], Yiwei Wu[1,2], Xiaoying Ye[1,2], Panpan Shi[1,2], Huiyu Li[1,2], Chang Liu[1,2], Lin Liu[1,2,6*] and Zhengmao Zhu[1,2,6*]

Affiliations

[1]State Key Laboratory of Medicinal Chemical Biology, Nankai University, 94 Weijin Road, Tianjin 300071, China

[2]Department of Cell Biology and Genetics, College of Life Sciences, Nankai University, 94 Weijin Road, Tianjin 300071, China

[3]Present address: Department of Traditional Chinese Medicine, Peking University Third Hospital, Beijing, 100191, China

[4]Present address: Institute of Translational Stem Cell Research, Helmholtz Diabetes Center, Helmholtz Zentrum Munchen, Munich, Germany

[5]Animal Resources Center, Nankai University, Tianjin, China.

[6]Academy for Advanced Interdisciplinary Studies, Nankai University

[#] These authors contributed equally.

[*] Correspondence: zhuzhengmao@nankai.edu.cn； liulin@nankai.edu.cn

2025-07-22; 2026-03-06

Summary

Oocyte number and quality decline greatly with age. Previously, we demonstrated that granulosa cells (GCs) from young mice could be effectively reprogrammed into chemically induced pluripotent stem cells (GC-CiPSCs), which can generate functional oocytes. Here, we investigated whether GCs isolated from reproductive-age mice could similarly generate germ cells. Old GC-CiPSCs reprogrammed from GCs isolated from reproductive-age mice exhibited pluripotent gene expression profiles comparable to those of embryonic stem cells and young GC-CiPSCs. However, old GC-CiPSCs displayed compromised mitochondrial function and a reduced capacity to differentiate into primordial germ cell-like cells (PGCLCs). Mitochondrial enhancement did not improve PGCLC induction efficiency in old GC-CiPSCs. However, inhibiting the ERK/MAPK signaling pathway improved the induction efficiency of PGCLCs from old GC-CiPSCs. These findings demonstrate functional deficits in generating PGCLCs from aged mouse GC-derived iPSCs and identify a strategy to improve PGCLC induction efficiency from senescent GCs.

Keywords: Senescence, Granulosa cells, Chemical reprogramming, Primordial germ cell, Mitochondria, ERK

Introduction

Ovarian function decreases with age due to reductions in oocyte quantity and quality (Findlay et al., 2015). This age-associated oocyte compromise involves multiple factors, including mitochondrial dysfunction, which manifests as reduced mitochondrial number and impaired energy production within the oocytes (Zhu et al., 2022). Granulosa cells (GCs), key somatic components of the ovarian follicle, play a critical role in orchestrating steroidogenesis, follicular maturation, and oocyte competence throughout folliculogenesis (Cavalcanti et al., 2023). GCs also exhibit stem cell-like properties (Coticchio et al., 2015; Hummitzsch et al., 2015). However, GCs, like oocytes, undergo cellular senescence with advancing reproductive age. This is characterized by mitochondrial dysfunction, telomere shortening, elevated oxidative stress, and a pro-inflammatory secretory phenotype (Tanaka et al., 2024).

The *in vitro* generation of functional oocytes presents a promising strategy to aid in fertility and endocrine functions (Gell and Clark, 2018; Tian et al., 2023; Tian et al., 2019a, c; Zhao et al., 2025). A key advancement is the development of culture systems capable of inducing primordial germ cell-like cells (PGCLCs) from pluripotent stem cells, which closely resemble endogenous primordial germ cells (PGCs). When aggregated with E12.5 embryonic gonadal somatic cells upon transplantation into the kidney or ovarian capsule, PGCLCs can differentiate into functional oocytes (Hayashi et al., 2012; Hayashi et al., 2011; Tian et al., 2019c). Notably, we previously demonstrated that chemical induction could be used to efficiently reprogram GCs isolated from young mice (2 to 3 months old) to a pluripotent state and generate chemically induced pluripotent stem cells (young GC-CiPSCs) without genetic modification (Tian et al., 2019c). Moreover, these young GC-CiPSCs could be successfully differentiated into PGCLCs and subsequently develop into functional oocytes capable of supporting full-term development and producing fertile offspring (Tian et al., 2019c).

The ERK/MAPK signaling cascade functions as a critical, context-dependent regulator of mammalian cell fate, orchestrating the divergent specification of somatic and germline lineages (Smith, 2017). Sustained ERK activity is a well-characterized driver of somatic differentiation, promoting lineage commitment through the transcriptional activation of mesodermal and other tissue-specific gene programs (Ying et al., 2008). In contrast, the establishment of PGCs necessitates the active suppression of ERK signaling. The pharmacological inhibition of MEK/ERK in pluripotent stem cell cultures efficiently redirects differentiation toward a PGC-like identity, concomitant with the upregulation of germline-specifying transcription factors (e.g., Prdm1, Tfap2c, and Dppa3) and the repression of somatic mesodermal markers (Kobayashi and Surani, 2018; Tonelli et al., 2025; Yu et al., 2022). This lineage bifurcation is further refined by temporally dynamic ERK modulation within the germline. Transient ERK reactivation is sequentially required for PGC proliferation, migratory capacity, and entry into meiosis (Grabole et al., 2013; Kimura et al., 2014).

However, a key question remains, “Can GCs obtained from reproductive-age mice (10

to 12 months old) be similarly reprogrammed into functional CiPSCs (old GC-CiPSCs), and do these old GC-CiPSCs retain the capacity to differentiate into PGCLCs and ultimately functional gametes?" Additionally, GCs are routinely aspirated and discarded during standard *in vitro* fertilization procedures, making them an attractive autologous cell source, even in older patients. In this study, we found that although old GC-CiPSCs exhibited pluripotency gene expression comparable to that of embryonic stem cells and young GC-CiPSCs, they displayed impaired mitochondrial function and reduced efficiency in PGCLC differentiation. Mitochondrial enhancement failed to rescue this deficiency. However, inhibiting the ERK/MAPK signaling pathway improved PGCLC induction efficiency.

Results

Mitochondrial dysfunction in oocytes from aging ovaries

We analyzed the oocyte transcriptomes of 10- to 12-month-old and 2- to 3-month-old mice. The germinal vesicle (GV) oocytes from 10- to 12-month-old mice (termed old GV oocytes) showed an upregulation of 2,069 genes and a downregulation of 1,499 genes (Figure S1A, B). Enrichment analysis revealed that these differentially expressed genes (DEGs) were mainly associated with neuron projection development, ribonucleoprotein complex biogenesis, and other cellular processes, with the downregulation of mitochondrial function-related pathways, such as mitochondrion organization and mitochondrial respiratory chain complex assembly (Figure S1C, D), indicating mitochondrial dysfunction.

Mito-Tracker Deep Red staining revealed that mitochondria clustered around the nucleus and appeared more rounded with a fragmented network in old GV oocytes, in contrast to the even distribution in GV oocytes from young mice (Figure S2A). JC-1 mitochondrial membrane potential staining revealed a significantly lower fluorescence intensity ratio (aggregates-red/monomers-green) in old GV oocytes than in control oocytes, indicating compromised mitochondrial membrane potential (Figure S2B, C). Reactive oxygen species (ROS) levels were elevated in old GV oocytes (Figure S2D, E), suggesting that mitochondrial dysfunction induced ROS accumulation (Peoples et al., 2019). Additionally, mitochondrial DNA (mtDNA) copy number and ATP content were significantly reduced in old GV oocytes (Figure S2F, G). These findings underscore mitochondrial dysfunction and compromised bioenergetic capacity as critical features of GV oocyte aging, consistent with previous findings (Alberico and Woods, 2021).

Mitochondrial dysfunction in GCs from aging ovaries

Unlike oocytes, which possess limited reprogramming potential, clinically discarded GCs offer an alternative source for generating PGCs. We isolated GCs from 2-month-old mice (termed young GCs) and 10- to 12-month-old mice (termed old GCs). Old GCs exhibited reduced proliferation (marked by PCNA) and increased senescence (marked by P16), indicating cellular aging (Figure 1A, B). Transcriptomic analysis revealed the downregulation of mitochondrial pathways, such as the positive regulation of mitophagy and the regulation of mitochondrial fission, in old GCs, with *DRP1* (a key mitochondrial fission regulator (Zhou et al., 2022)) significantly reduced in old GCs (Figures 1C and S3D, E). Additionally, old GCs had lower mtDNA copy numbers and ATP content (Figure 1D, E).

Mitochondria in old GCs labeled with TOMM20 were more dispersed throughout the cytoplasm than their young counterparts, indicating altered mitochondrial dynamics (Figure 1F). This altered distribution may affect the ability of mitochondria to supply energy to the nucleus (Hamilton et al., 2020; Varum et al., 2011). The ROS assay results showed that old GCs had greater ROS accumulation (Figure 1G). JC-1 staining revealed reduced mitochondrial membrane potential in old GCs (Figure 1H), indicating compromised mitochondrial function.

Transcriptomic analysis revealed 315 upregulated and 247 downregulated genes in old GCs (Figure S3A), including aging-associated genes, such as *Ccl2*, *Eln*, and *Serpine1* (Aging Atlas, 2021) (Figure S3B). The enrichment analysis of the DEGs revealed the significant activation of immune-related pathways, such as the inflammatory response and the virus response, which is consistent with ovarian senescence (Minhas et al., 2021; Yang et al., 2024; Zhang et al., 2023) (Figure S3C). These data highlight mitochondrial dysfunction and cellular senescence as key characteristics of aging GCs.

Generation of CiPSCs from the senescent GCs of reproductive-age mice

Senescent GCs were isolated and reprogrammed into CiPSCs (termed old GC-CiPSCs) using an established method (Fu et al., 2018; Zhao et al., 2015) and compared with CiPSCs derived from the GCs of 2-month-old mice (termed young GC-CiPSCs) (Figure 2A–C). Chromosomal stability was confirmed by chromosome karyotype analysis (Figure S4A). The expression of pluripotency markers (*Oct4*, *Nanog*, and *Sox2*) did not significantly differ between ESCs, young GC-CiPSCs, and old GC-CiPSCs (Figures 2D and S4B, C). Transcriptomic analysis revealed 65 upregulated and 105 downregulated genes in old GC-CiPSCs compared with young GC-CiPSCs (Figures 2D and S4D). Enrichment analysis revealed that the upregulated DEGs were associated with calcium ion transmembrane transporter activity and ERK1/2 cascade regulation, whereas the downregulated DEGs were associated with embryonic placenta development and WNT ligand biogenesis and trafficking (Figure 2E, F). Notably, the Hippo pathway, which is crucial for stem cell function, was also enriched within the WNT ligand biogenesis and trafficking pathways (Figure S4E).

Induction of PGCLCs from old and young GC-CiPSCs

PGCLCs were induced from CiPSCs using an established protocol (Hayashi et al., 2012). Young GC-CiPSCs efficiently differentiated into epiblast-like cells (EpiLCs) and subsequently into PGCLCs (Figure 3A), with an efficiency comparable to that of ESCs, as confirmed by flow cytometry analysis (FACS). In contrast, the induction efficiency of old GC-CiPSCs into PGCLCs was significantly lower (Figure 3B, C). Immunofluorescence revealed decreased STELLA (germ cell marker) and increased GATA4 (somatic cell marker) in old GC-CiPSC-derived embryoid bodies (EBs) (Figure 3D, E). These findings indicate the reduced ability of old GC-CiPSCs to differentiate into PGCLCs.

PGCLC induction by targeting mitochondrial function

Previous studies demonstrated abnormal mitochondrial function in aged GCs (Tanaka et al., 2024). We assessed mitochondrial function in old GC-CiPSCs compared with young GC-CiPSCs. Mito-Tracker Deep Red staining revealed that the mitochondria in ESCs and young GC-CiPSCs were predominantly round, whereas some of the mitochondria in old GC-CiPSCs were shorter and rod-shaped (Figure 4A). Notably, the ATP content was higher in old GC-CiPSCs (Figure 4B), despite the mtDNA copy number being significantly lower than in ESCs and young GC-CiPSCs (Figure 4C). This low-ATP, glycolysis-dominated state is considered metabolically “youthful” and is tightly linked to the maintenance of pluripotency and germline competency (Folmes

et al., 2011; Prigione et al., 2010; Zhou et al., 2012). JC-1 staining revealed a lower fluorescence intensity ratio (aggregates-red/monomers-green) in old GC-CiPSCs (Figure 4D). Abnormal mitochondrial fission and fusion can impair germline transmission in ESCs (Hayashi et al., 2011; Zhong et al., 2019). Western blotting revealed decreases in DRP1, a key protein essential for mitochondrial fission, in old GC-CiPSCs (Figure 4E, F). Additionally, ROS levels were higher in old GC-CiPSCs (Figure 4G), further indicating mitochondrial dysfunction.

We aimed to increase the induction efficiency of PGCLCs from old GC-CiPSCs and improve mitochondrial function using antioxidant treatments, such as nicotinamide mononucleotide (NMN), alpha-ketoglutarate (α-KG), coenzyme Q10, vitamins C and E, and flavonoids, which are known to promote mitochondrial function (Ben-Meir et al., 2015; Bertoldo et al., 2020). In the initial experiment, 50 or 100 μM α-KG was added to the culture medium of old GC-CiPSCs for three generations, and the same concentrations of NMN and α-KG were also added during PGCLC induction. Optical microscopy revealed that both young GC-CiPSCs and old GC-CiPSCs, as well as those supplemented with NMN and α-KG, could differentiate into EpiLCs and subsequently form EBs (Figure S5A). However, flow cytometry analysis revealed that adding NMN or α-KG during PGCLC induction did not improve induction efficiency in old GC-CiPSCs (Figure S5A). Further analysis confirmed the significant downregulation of DRP1 in old GC-CiPSCs (Figure S5B, C). Because mitochondrial dynamics are essential for stem cell function (Zhong et al., 2019), we explored whether enhancing mitochondrial fission could improve induction efficiency. Old GC-CiPSCs were treated with sodium palmitate (NaPA) (Qin et al., 2019) for three generations to activate DRP1 expression and activity (Figure S5D, S5E). Although DRP1 was activated, the FACS analysis of differentiated EBs showed that this activation did not increase the induction efficiency of PGCLCs from old GC-CiPSCs (Figure S5F, G). These results suggest that while mitochondrial function affects CiPSC quality, DRP1 activation alone is insufficient to overcome age-related limitations in PGCLC induction efficiency.

Increasing PGCLC induction by modulating signal transduction

The transcriptomic analysis of young and old GC-CiPSCs revealed that the downregulated genes in old GC-CiPSCs were enriched in the Hippo signaling pathway. Western blotting confirmed decreased active YAP levels in these cells (Figure S5H). We treated old GC-CiPSCs with XMU-MP-1 for three generations to investigate the role of YAP in PGC lineage specification. XMU-MP-1 activates the downstream effector YAP protein and promotes cell growth by inhibiting MST1/2 activity (Ma et al., 2019). This treatment increased active YAP levels (Figure S5I) and resulted in a modest improvement in PGCLC induction efficiency (approximately 1–2%) in old GC-CiPSCs (Figure S5J).

Additionally, genes upregulated in old GC-CiPSCs were enriched in the ERK-related signaling pathway. MAPK cascade signaling was also upregulated in PGCLCs derived from old GC-CiPSCs. We administered 1 μM PD0325901 during the induction process of old GC-CiPSCs into PGCLCs to test whether inhibiting

ERK/MAPK signaling could improve PGCLC induction in old GC-CiPSCs. Western blot analysis confirmed that PD0325901 treatment reduced p-ERK levels in EBs (Figure 5A). FACS analysis revealed that PD0325901 treatment nearly doubled induction efficiency, increasing it by 2–3% (Figure 5B). Inhibiting MAPK/ERK signaling increased the number of germ cell markers, as determined by STELLA and VASA analyses, while the level of the somatic cell marker GATA4 decreased in EBs derived from old GC-CiPSCs (Figure 5C–E). These results suggest that inhibiting the MAPK/ERK signaling pathway can enhance PGCLC induction in old GC-CiPSCs, suggesting a potential strategy to overcome age-related limitations in germ cell differentiation.

Comparative transcriptomic analysis of PGCLCs derived from young and old GC-CiPSCs

We performed RNA-sequencing (RNA-seq) analysis to compare PGCLCs derived from young and old GC-CiPSCs (Figure 6A). The expression of key PGC genes (*prdm14*, *tfap2c*, *itgb3*, and *ifitm3*) in these PGCLCs was comparable to that in E12.5 PGCs (Figure 6B). Kyoto Encyclopedia of Genes and Genomes (KEGG) and Gene Ontology (GO) analyses revealed that the genes upregulated in PGCLCs from old GC-CiPSCs were enriched in the transforming growth factor-β signaling pathway and biological processes related to MAPK cascade regulation (Figure 6B). Consistently, previous studies have suggested that inhibiting MAPK signaling promotes specialization toward PGCLCs (Jia et al., 2008; Kimura et al., 2014; Tian et al., 2023; Zhu et al., 2023). In contrast, PGCLCs from young GC-CiPSCs were upregulated in processes related to the regulation of bone morphogenic protein (BMP) signaling, oogenesis, female gamete generation, and gonad development (Figure 6C), suggesting that old GC-CiPSCs have a compromised capacity for PGC differentiation.

We treated PGCLCs derived from old GC-CiPSCs with PD0325901 to assess the effect of MAPK pathway inhibition. PGCLCs derived from young GC-CiPSCs served as controls. This treatment preventedthe expression of many genes in PGCLCs from old GC-CiPSCs (Figure 6D). GO enrichment analysis revealed that MAPK cascade regulation was inhibited by PD0325901 treatment and that PD0325901 reversed key biological processes, including the Alzheimer's and Huntington's disease pathways, WNT signaling regulation, the meiosis cell cycle, and responses to retinoic acid (Figure 6E, F). Moreover, inhibiting the ERK/MAPK pathway downregulated genes related to cellular senescence in PGCLCs from old GC-CiPSCs, whereas upregulated genes were associated with mitochondrial metabolism and other metabolic processes (Figure 6E, F). These findings suggest that inhibiting ERK/MAPK signaling may enhance mitochondrial function and mitigate aging-related characteristics, thereby improving the ability of old GC-CiPSCs to differentiate into PGCLCs.

Discussion

Previously, we successfully generated functional oocytes with genomic stability that produced fertile pups from the GCs of young mice using a chemical reprogramming approach and PGCLC induction (Hayashi et al., 2012; Tian et al., 2019a, c). In this study, we extended these findings by successfully deriving CiPSCs from senescent GCs in reproductive-age mice. However, we observed that these derived cells exhibited impaired mitochondrial function and a reduced capacity to differentiate into PGCLCs. This finding aligns with previous studies on disease-specific human iPSCs, which often retain disease phenotypes that limit their redifferentiation potential (Wahlestedt et al., 2014).

Furthermore, we found that targeting mitochondrial function using NMN and α-KG did not enhance PGCLC induction efficiency in old GC-CiPSCs. Both NMN and α-KG have been previously shown to promote mitochondrial function (Ben-Meir et al., 2015; Bertoldo et al., 2020; Zhu et al., 2022). We observed that old GC-CiPSCs supplemented with NMN and α-KG could differentiate into EpiLCs and subsequently form EBs. However, these supplements did not improve the induction efficiency of PGCLCs from old GC-CiPSCs. These results indicate that although mitochondrial function is essential for differentiation, its restoration alone is insufficient to rescue the age-related decline in the reprogramming potential of these cells. We also found that the mitochondria in ESCs and young GC-CiPSCs were predominantly round, whereas in old GC-CiPSCs, some mitochondria were shorter and rod-shaped, indicating altered morphology. Additionally, DRP1, a protein essential for mitochondrial fission, was significantly downregulated in old GC-CiPSCs. Abnormal mitochondrial fission and fusion have previously been shown to impair germline transmission in embryonic stem cells (Ishihara et al., 2009; Zhong et al., 2019), which may explain the reduced differentiation ability of old GC-CiPSCs. Although NaPA treatment activated DRP1 expression and activity, it did not increase the efficiency of PGCLC induction. These findings suggest that the reduced differentiation ability of old GC-CiPSCs is not attributable to mitochondrial dysfunction alone; rather, it is likely a multifactorial process compounded by nuclear aging, as old GCs exhibit both mitochondrial damage and nuclear aging.

Finally, the gene expression analysis of old GC-CiPSCs revealed a downregulation of genes involved in embryonic placenta development and WNT ligand biogenesis and trafficking and an upregulation of genes associated with the regulation of calcium ion transmembrane transporter activity and the regulation of the ERK1/2 cascade. These findings are consistent with previous studies, as the WNT signaling pathway is crucial for the ability of epiblast cells to induce germline determinants downstream of BMP4, ultimately leading to PGC formation (Aramaki et al., 2013; Ohinata et al., 2009). Additionally, activating the MAPK/ERK pathway has been shown to promote somatic cell lineage differentiation while suppressing germ cell specification and development (Grabole et al., 2013). The altered expression profile in old GC-CiPSCs aligns with the observed low efficiency of PGCLC induction. Inhibiting the ERK/MAPK signaling pathway enhanced PGCLC induction in old GC-CiPSCs, suggesting that the

aberrant activation of this signaling pathway may be a key barrier to efficient germ cell differentiation in aged GC-CiPSCs.

ERK/MAPK pathway inhibition may enhance the differentiation of aged GC-CiPSCs into primordial germ cell-like cells by improving mitochondrial function. The hyperactivation of ERK signaling impairs mitochondrial biogenesis, increases oxidative stress, and disrupts cellular energy metabolism, whereas ERK inhibition can restore OXPHOS, reduce ROS levels, and preserve mitochondrial integrity (Ma, 2013). Because PGC specification requires a metabolic shift from glycolysis toward OXPHOS, ERK inhibition via PD0325901 may activate mitochondrial biogenesis pathways involving the PGC-1α/NRF1-TFAM axis, facilitate tricarboxylic acid cycle-driven epigenetic remodeling, and enhance mitochondrial quality control through PINK1/Parkin-mediated mitophagy (Carey et al., 2015; Narendra et al., 2008). Given that CiPSCs derived from aged GCs exhibit intrinsic mitochondrial defects, metabolic restoration by inhibiting ERK/MAPK may create a permissive bioenergetic state conducive to acquiring germ cell fate.

Our transcriptomic analysis demonstrated a significant upregulation of Dnmt3a and HDAC6 in CiPS cells derived from old GCs (Figure S6), suggesting an altered epigenetic regulatory state. During GC-to-PSC reprogramming, epigenetic resetting is facilitated by small molecules such as 5-aza-dC and VPA, which promote DNA demethylation and histone acetylation to silence somatic programs and enable pluripotency acquisition. However, elevated Dnmt3a and HDAC6 expression in old-GC-CiPS cells may promote locus-specific DNA hypermethylation and histone hypoacetylation, thereby restricting the activation of genes critical for successful reprogramming. This epigenetic constraint is likely more detrimental during PGCLC induction, a process characterized by extensive DNA methylation reprogramming, ultimately leading to reduced induction efficiency. Collectively, these findings suggest that age-associated epigenetic dysregulation contributes to impaired reprogramming and germline competence in old GCs.

While this study provides a proof-of-principle demonstration of the feasibility of generating PGCLCs from aged GCs, several limitations should be acknowledged. Notably, the mouse GCs used lacked fluorescent pluripotency reporters, which precluded the precise fluorescence-based quantification of all reprogramming events. Furthermore, while we have established induction potential, rigorous functional analyses remain a critical next step to fully validate the quality and potential of PGCLCs derived from aged GC-CiPSCs.

In conclusion, our study underscores the effect of cellular aging on the reprogramming and differentiation potential of GC-derived CiPSCs. These findings highlight that both mitochondrial dysfunction and nuclear aging play pivotal roles in reducing the capacity of aged GCs to differentiate into germ cells. Targeting mitochondrial function alone was insufficient to restore the differentiation potential of old GC-CiPSCs, indicating that interventions addressing both mitochondrial and nuclear aging may be necessary. Furthermore, the altered expression of key signaling

pathways, such as the WNT and MAPK/ERK pathways, underscores the complexity of the differentiation process and offers potential avenues for enhancing the efficiency of germ cell derivation from old GC-iPSCs. Future studies focusing on mitochondrial rejuvenation, nuclear reprogramming, and pathway modulation could provide valuable insight into improving the generation of germ cells from aged somatic cells, thereby offering new strategies for restoring age-related endocrine function.

Methods

Animal care and use

This study was conducted with the approval of the Nankai University Animal Care and Use Committee, ensuring compliance with all relevant regulations. The mice were housed individually in ventilated cages in a sterile environment with a standard 12-h light/dark cycle. C57BL/6NCrSlc (B6) mice aged 2–3 months and 10–12 months were purchased from Beijing Vital River Laboratory Animal Technology Co., Ltd.

Granulosa cell isolation and culture

Granulosa cells were isolated from 8 to 12-week-old female C57BL/6 mice primed with 5 IU PMSG via intraperitoneal injection 48 hours prior to euthanization. Under stereomicroscopic guidance (Nikon SMZ18), preantral and early antral follicles were mechanically dissociated from the ovarian cortex using needle puncture. This selective puncture strategy preferentially released GCs from the mural layer of preantral and early antral follicles. Cell clumps and oocytes were removed by filtering the cell suspensions through a 40 μm nylon cell strainer (BD Biosciences, New York,; no. 352340) (Tian et al., 2019b). Primary GCs were cultured in S/L medium for 6 days until reaching a density of 1×10^5 cells per well in a six-well plate.

Induction of CiPSCs from granulosa cells

Culture processes were conducted as previously described (Tian et al., 2019a, c). Primary cultured GCs were maintained for 6 days in S/L medium until they reached a density of 10^5 cells per well in a six-well plate. On day 0 (induction start), the medium was replaced with stage 1 induction medium for CiPSC generation.

From days 0 to 12 of differentiation (the first part of stage 1), the induction medium contained 100 ng mL^{-1} bFGF (PeproTech), 0.5 mM VPA (Sigma), 20 mM CHIR99021 (Selleck), 10 mM RepSox (Selleck), 5 mM Parnate (Sigma), 50 mM forskolin (Selleck), 0.05 mM AM580 (Tocris), and 5 mM EPZ004777 (Selleck). During days 12 to 16 (the second part of stage 1), the concentrations of bFGF, CHIR99021, and forskolin were reduced to 25 ng mL^{-1}, 10 mM, and 10 mM. From days 16 to 28 (stage 2), the induction medium consisted of 25 ng mL^{-1} bFGF, 0.5 mM VPA, 10 mM CHIR99021, 10 mM Repsox, 5 mM Parnate, 10 mM forskolin, 0.05 mM AM580, 0.05 mM DZNep (Selleck), 0.5 mM 5-aza-dC (Sigma), 5 mM SGC0946 (Selleck), and 7 mM crotonic sodium (CS, crotonic acid (Millipore)), adjusted to pH 7.0 with 1 N NaOH. On day 28 (stage 3), the culture was transferred into 2i/L medium, which consisted of a 1:1 mixture of Dulbecco's modified Eagle medium/F12 (Invitrogen) supplemented with N2 and B27 (Invitrogen), 1 mM L-glutamine, 1% nonessential amino acid stock, 50 units mL^{-1} penicillin and 50 mg mL^{-1} streptomycin, 0.1 mM b-mercaptoethanol, 1000 IU mL^{-1} IF, 1 mM PD0325901, and 3 mM CHIR99021. Between days 8 and 3, Oct4 green fluorescent protein-positive primary colonies of CiPSCs derived from GCs emerged. These colonies were picked and expanded using S/L + 2i media on feeder layers.

Induction of PGC-like cells

PGCLC induction from ESCs/CiPSCs was performed following previously established methods (Hayashi et al., 2012; Hayashi et al., 2011). ESCs and CiPSCs at

passages 8–10 were cultured in feeder-free N2B27+2iL medium (N2B27 medium containing 1,000 IU/mL IF, 3 μmol/L CHIR99021, and 0.4 μmol/L PD0325901) for 3–5 passages. EpiLCs were induced by plating 1×10^5 female ESCs/CiPSCs in 12-well plates coated with human plasma fibronectin (FN, 16.7 mg/mL, Millipore) in N2B27 medium supplemented with activin A (20 ng$^{/mL}$, PeproTech), bFGF (12 ng$^{/mL}$), and 1% KSR for 44–46 hours, with daily medium changes. PGCLCs were induced by plating 3×10^3 EpiLCs into low-cell-binding U-bottom 96-well Lipidure-Coat plates (Corning) and cultured in GK15 medium (GMEM (Invitrogen) with 15% KSR, 1 mM sodium pyruvate, 1 mM L-glutamine, 1% nonessential amino acid stock, 50 units mL^{-1} penicillin, 50 mg mL^{-1} streptomycin, and 0.1 mM β-mercaptoethanol) for 6 days under floating conditions. The induction medium contained BMP4 (500 ng/mL, PeproTech), 1000 IU/mL IF, SCF (100 ng$^{/mL}$, PeproTech), and EGF (50 ng/mL, PeproTech).

Integrin-β3 (CD61)- and SSEA1-double-positive PGCLCs were sorted using flow cytometry. Dissociated cells were incubated with anti-integrin-β3 (CD61) antibody (BioLegend, 104307) and anti-SSEA1 antibody (eBioscience, 508813-42) conjugated with phycoerythrin (red color) and Alexa Fluor 647, respectively. After washing in phosphate-buffered saline (PBS) with 0.1% bovine serum albumin (BSA; Sigma), the cells were analyzed using a flow cytometer (Aria III; BD Biosciences).

Production of chimeras

Approximately 10–15 ESCs or CiPSCs (passages 8–12) were injected into 4 to 8-cell BALB/c mouse embryos using a Piezo injector. The injected embryos were cultured overnight in $KSOM_{AA}$ medium. Blastocysts were then transferred to the uterine horns of surrogate mice at 2.5 days post-coitum (dpc). The pregnant females delivered pups naturally at approximately 19.5 dpc. Chimeric pups were identified by coat color.

Collection of mouse oocytes

Superovulation was performed in 6- to 8-week-old female mice by administering 5 IU of pregnant mare serum gonadotropin (PMSG). GV oocytes were collected 24 hours postinjection. The ovaries of 6- to 8-week-old female mice were dissected using ophthalmic scissors, and the oocytes were identified by stereomicroscopy. The samples were then washed three times with M2 medium (Sigma, USA).

Immunofluorescence microscopy

The cells were washed twice with PBS and fixed in freshly prepared 3.7% paraformaldehyde for 30 minutes at 4°C. Following fixation, the cells were washed once with PBS and permeabilized with 0.1% Triton X-100 in blocking solution (3% goat serum plus 0.1% BSA in PBS) for 30 minutes at room temperature. The cells were then washed three times with PBS and incubated in blocking solution for 2 hours. Primary antibodies against Oct4 (sc5279, Santa Cruz), Nanog (ab80892, Abcam), SSEA1 (MAB4301, Millipore), Foxl2 (ab5096, Abcam), Drp1 (ab184247, Abcam), and Tomm20 (ab186735, Abcam) were added and incubated overnight at 4°C. Then, the cells were washed three times (15 minutes each) with blocking solution and incubated for 2 hours with secondary antibodies at room temperature. The secondary antibodies used were as follows: fluorescein isothiocyanate-conjugated goat

anti-mouse IgG (H + L), Alexa Fluor 594-conjugated goat anti-rabbit IgG (H + L), and Alexa Fluor 594-conjugated donkey anti-goat IgG (H + L). All secondary antibodies were diluted 1:200 in blocking solution. After washing, the samples were counterstained with 0.5 mg mL^{-1} DAPI (Roche) in Vectashield (Vector) mounting medium. Fluorescence was detected and imaged using an Axio Imager Z2 or LSM 800 with an Airyscan fluorescence microscope (Carl Zeiss).

Gene expression analysis by real-time quantitative PCR

Total RNA was extracted using an RNA mini kit (Qiagen) and treated with DNase I (Qiagen). cDNA was generated from 2 μg of RNA using oligo (dT)18 primers (Takara) and M-MLV reverse transcriptase (Invitrogen). Real-time quantitative PCR (RT-qPCR) was performed in duplicate using FS Universal SYBR Green Master (Roche) on an iCycler MyiQ2 Detection System (Bio-Rad). The target genes and internal controls were amplified on the same plate. Each sample was tested in triplicate and normalized against *Gapdh* as the internal control. Amplification included an initial denaturation at 95°C for 10 minutes, followed by 40 cycles of denaturation at 95°C for 15 seconds, annealing and elongation at 58°C for 1 minute, and a final dissociation curve cycle at 55–95°C. Relative quantification of the target gene was determined by comparing the threshold cycles.

Western blots

The cells were washed twice with PBS, collected, and lysed in cell lysis buffer on ice for 30 minutes, followed by sonication for 1 minute at 60% amplitude with 2-second intervals. After centrifugation at 10,000 × *g* at 4°C for 10 min, the supernatant was transferred to new tubes. Protein concentrations were measured using the bicinchoninic acid assay. Protein samples were boiled in sodium dodecyl sulfate (SDS) sample buffer at 95°C for 10 minutes. Total protein (10 μg) from each cell extract was resolved by 10% Acr-Bis SDS-polyacrylamide gel electrophoresis and transferred to polyvinylidene difluoride membranes (Millipore). Nonspecific binding was blocked by incubating the membranes in 5% skim milk or 5% BSA in TBST at room temperature for 2 hours. The blots were then probed overnight at 4°C with primary antibodies against Oct4, Nanog, Lin28, Tomm20, Drp1, or β-actin (loading control). Immunoreactivity bands were probed for 2 hours at room temperature with the appropriate horseradish peroxidase (HRP)-conjugated secondary antibodies, HRP-conjugated goat anti-rabbit IgG, or HRP-conjugated goat anti-mouse IgG (H + L). The protein bands were detected using a chemiluminescent HRP substrate (WBKLS0500, Millipore).

Active mitochondrial staining

Oocytes and cells were incubated with MitoTracker® Deep Red FM (1:1000, M22426, Invitrogen) at 37°C in 5% CO_2 for 30 minutes. Following three washes with M2 medium, the DNA was stained with PBS containing 10 μg mL^{-1} Hoechst 33342. The samples were then observed by confocal microscopy.

Mitochondrial DNA copy number measurement using real-time qPCR

A total of 20 oocytes were transferred to 20 μL of lysis buffer (50 mm Tris-HCl, 200 μg mL^{-1} proteinase K, and 0.5% Triton X-100) and incubated at 55°C for 2 hours.

Real-time PCR was performed to quantify the mtDNA copy number. Each experiment was independently repeated at least three times. The levels of the mitochondrial *COI I* gene (forward primer: 5'-CTAACAGACCGCAACCTCAAC-3'; reverse primer: 5'-TCCGAAGCCTGGTAGGATAAG-3') were normalized to those of the nuclear *18S rRNA* gene (forward primer: 5'-TGTGATGCCCTTAGATGTCC-3'; reverse primer: 5'-TGGGGTTCAGCGGGTTAC-3').

Assay of mitochondrial membrane potential

Oocytes and cells were incubated with JC-1 (Beyotime, China) at 37°C in 5% CO_2 for 30 minutes. Membrane potential was measured as the ratio of red fluorescence (J-aggregates) to green fluorescence (J-monomers) using confocal microscopy as previously described (Ben-Meir et al., 2015).

Reactive oxygen species measurement

ROS levels in the oocytes and cells were measured using an ROS assay kit (Beyotime, China). Oocytes were incubated in M2 medium containing 10 μM DCFH-DA at 37°C for 20 minutes, followed by three washes with M2 medium. The cells were incubated in S/L serum-free medium supplemented with 10 μM DCFH-DA at 37°C for 20 minutes, followed by three washes with the same medium. The fluorescence signals were detected by confocal microscopy.

ATP measurement

The ATP content was measured using an ATP determination kit (Molecular Probes, USA) according to the manufacturer's instructions. Cells or 30 oocytes were collected in 30 μL of lysis buffer. Then, 10 μL of each sample was added to each well of a 96-well plate, and 100 μL of standard reaction mixture was added to each well. The light intensity was set to 1 for the control group. The relative intensity of the treatment group was measured and compared with that of the control group.

Library preparation and sequencing

A total of 500 cells were isolated by FACS in 1.5 mL tubes and then transferred into 200 μL PCR tubes (Axygen, PCR-0208-C). Two microliters of cell lysis buffer containing 0.2% Triton X-100, 0.05 μL of recombinant RNase inhibitor (2313A, Contech), 1 μL of 10 μM oligo-dT primer, and 1 μL of 10 mM dNTPs were added to each PCR tube. Single-cell cDNA was synthesized according to the SMART-seq2 protocol with minor modifications (Picelli et al., 2014). The mRNA in each PCR tube was suspended in 10 μL of RT mix containing 0.25 μL of 100× template-switching oligonucleotide (TSO) primer (5′-AAGCAGTGGTATCAACGCAGAGTACATrGrG+G-3′), 1 μL of 10 mM dNTPs (11969064001, Roche), 0.06 μL of 1 M $MgCl_2$ (AM9530G, Ambion), 2 μL of 5 M betaine (77507, Affymetrix), 0.5 μL of 100 mM dithiothreitol, 2 μL of 5× Superscript II First-Strand Buffer, 0.5 μL of 200 U μL^{-1} Super Script II reverse transcriptase (18064014, Invitrogen), 0.25 μL of 40 U μL^{-1} RNase inhibitor (2313A, Clontech), and 3.44 μL of nuclease-free water (W4502-1 L, Sigma-Aldrich). The tubes were vortexed, followed by reverse transcription at 42°C for 90 minutes, 10 cycles at 50°C for 2 minutes and 42°C for 2 minutes, and reverse transcriptase inactivation at 70°C for 15 minutes. Following reverse transcription, 15 μL of PCR preamplification mix

was added to each tube, including 0.5 μL of 10 μM PCR preamplification primer, 12.5 μL of 2× KAPA HiFi Mix (KK2601, KAPA Biosystems), and 2 μL of nuclease-free water. The final PCR volume was 25 μL. The preamplification program was as follows: 98°C for 3 minutes; 22 cycles of 98°C for 15 seconds, 67°C for 20 seconds, and 72°C for 6 minutes; and a final extension at 72°C for 5 minutes. Libraries were then prepared using the TruePrep DNA Library Prep Kit V2 for Illumina® (TD503-02; Vazyme Biotech) according to the manufacturer's instructions. The samples were barcoded and multiplexed for sequencing using a 150-bp paired-end sequencing strategy on an Illumina HiSeq platform.

RNA-sequencing analysis

Total RNA was extracted from ESCs, young/old GC-CiPSCs, and young/old GCs. RNA-seq library preparation was performed by Biomarker Technologies. Sequencing libraries were constructed, and paired-end mRNA-seq data with read lengths of 150 bp were generated, with two or three biological replicates for each cell line. The raw reads were first aligned to the mouse reference genome (mm10) using STAR software with default parameters. The expression matrix was generated using FeatureCounts software (Ding et al., 2025; Liao et al., 2014). DEGs were calculated using the R package DEseq2 (Dobin and Gingeras, 2015). Expression levels are presented as counts per million (CPM). DEGs were identified based on the following criteria: absolute fold-change > 1.5 and false discovery rate < 0.05. We used the Metascape website (https://metascape.org/gp/index.html#/main/step1) to compare the functions of the DEGs in the five cell types.

Statistical analysis

Statistics were analyzed using StatView software from SAS Institute Inc. (Cary, NC, USA). Data were analyzed using a two-tailed unpaired Student's *t*-test to compare two groups and are expressed as mean ± SD. P-values of less than 0.05 were considered significant. N values are described in the corresponding figure legends. FlowJo was used to analyze FACS data. GraphPad Prism was used to generate graphs.

Data and code availability

The RNA-sequencing data generated in this study have been deposited in the NCBI database under accession number GSE285567.

Acknowledgments

This work was supported by the National Key R&D Program of China (2022YFA1103800 and 2018YFC1003004) and the National Natural Science Foundation of China (82230052 and 32030033). We thank LetPub (www.letpub.com.cn) for its linguistic assistance during the preparation of this manuscript.

Compliance and ethics

All authors declare no competing interests. All authors state that they conformed with the Helsinki Declaration of 1975 (as revised in 2008) concerning animal rights. All animal experiments were performed in accordance with protocols approved by the Institutional Animal Care and Use Committee of Nankai University (License No.

20140006).

Author Contributions

D.H.L.L. and Z.Z. designed the experiments. D.H. and K.J. conducted the major experiments, analyzed the data, and prepared the manuscript. Y.G., C.T., X.S., J.L., Y.W., X.Y., P.S., H.L., and C.L. conducted part of the experiments or provided materials. L.L. conceived the project, and L.L. and Z.Z. revised the manuscript.

References

Aging Atlas, C. (2021). Aging Atlas: a multi-omics database for aging biology. Nucleic Acids Res *49*, D825-D830.

Alberico, H.C., and Woods, D.C. (2021). Role of Granulosa Cells in the Aging Ovarian Landscape: A Focus on Mitochondrial and Metabolic Function. Front Physiol *12*, 800739.

Aramaki, S., Hayashi, K., Kurimoto, K., Ohta, H., Yabuta, Y., Iwanari, H., Mochizuki, Y., Hamakubo, T., Kato, Y., Shirahige, K., et al. (2013). A mesodermal factor, T, specifies mouse germ cell fate by directly activating germline determinants. Dev Cell *27*, 516-529.

Ben-Meir, A., Burstein, E., Borrego-Alvarez, A., Chong, J., Wong, E., Yavorska, T., Naranian, T., Chi, M., Wang, Y., Bentov, Y., et al. (2015). Coenzyme Q10 restores oocyte mitochondrial function and fertility during reproductive aging. Aging Cell *14*, 887-895.

Bertoldo, M.J., Listijono, D.R., Ho, W.J., Riepsamen, A.H., Goss, D.M., Richani, D., Jin, X.L., Mahbub, S., Campbell, J.M., Habibalahi, A., et al. (2020). NAD(+) Repletion Rescues Female Fertility during Reproductive Aging. Cell Rep *30*, 1670-1681 e1677.

Carey, B.W., Finley, L.W., Cross, J.R., Allis, C.D., and Thompson, C.B. (2015). Intracellular α-ketoglutarate maintains the pluripotency of embryonic stem cells. Nature *518*, 413-416.

Cavalcanti, G.S., Carvalho, K.C., Ferreira, C.D.S., Alvarez, P.A.C., Monteleone, P.A.A., Baracat, E.C., and Soares Junior, J.M. (2023). Granulosa cells and follicular development: a brief review. Rev Assoc Med Bras (1992) *69*, e20230175.

Coticchio, G., Dal Canto, M., Mignini Renzini, M., Guglielmo, M.C., Brambillasca, F., Turchi, D., Novara, P.V., and Fadini, R. (2015). Oocyte maturation: gamete-somatic cells interactions, meiotic resumption, cytoskeletal dynamics and cytoplasmic reorganization. Hum Reprod Update *21*, 427-454.

Ding, R., Yang, J., Yan, C., Yin, D., Zhang, D., and Jiang, W. (2025). Ribo-seq provides additional evidence for cytoplasm-translated mitochondrial DNA-encoded ORFs. Sci China Life Sci *68*, 3407-3409.

Dobin, A., and Gingeras, T.R. (2015). Mapping RNA-seq Reads with STAR. Curr Protoc Bioinformatics *51*, 11 14 11-11 14 19.

Findlay, J.K., Hutt, K.J., Hickey, M., and Anderson, R.A. (2015). How Is the Number of Primordial Follicles in the Ovarian Reserve Established? Biol Reprod *93*, 111.

Folmes, C.D., Nelson, T.J., Martinez-Fernandez, A., Arrell, D.K., Lindor, J.Z., Dzeja, P.P., Ikeda, Y., Perez-Terzic, C., and Terzic, A. (2011). Somatic oxidative bioenergetics transitions into pluripotency-dependent glycolysis to facilitate nuclear reprogramming. Cell Metab *14*, 264-271.

Fu, H., Tian, C.L., Ye, X., Sheng, X., Wang, H., Liu, Y., and Liu, L. (2018). Dynamics of Telomere Rejuvenation during Chemical Induction to Pluripotent Stem Cells. Stem Cell Reports *11*, 70-87.

Gell, J.J., and Clark, A.T. (2018). Restoring Fertility with Human Induced Pluripotent Stem Cells: Are We There Yet? Cell Stem Cell *23*, 777-779.

Grabole, N., Tischler, J., Hackett, J.A., Kim, S., Tang, F., Leitch, H.G., Magnusdottir, E., and Surani, M.A. (2013). Prdm14 promotes germline fate and naive pluripotency by repressing FGF signalling and DNA methylation. EMBO Rep *14*, 629-637.

Hamilton, J., Brustovetsky, T., Sridhar, A., Pan, Y., Cummins, T.R., Meyer, J.S., and Brustovetsky, N. (2020). Energy Metabolism and Mitochondrial Superoxide Anion Production in Pre-symptomatic Striatal Neurons Derived from Human-Induced Pluripotent Stem Cells Expressing Mutant Huntingtin. Mol Neurobiol *57*, 668-684.

Hayashi, K., Ogushi, S., Kurimoto, K., Shimamoto, S., Ohta, H., and Saitou, M. (2012). Offspring from oocytes derived from in vitro primordial germ cell-like cells in mice. Science *338*, 971-975.

Hayashi, K., Ohta, H., Kurimoto, K., Aramaki, S., and Saitou, M. (2011). Reconstitution of the mouse germ cell specification pathway in culture by pluripotent stem cells. Cell *146*, 519-532.

Hummitzsch, K., Anderson, R.A., Wilhelm, D., Wu, J., Telfer, E.E., Russell, D.L., Robertson, S.A., and Rodgers, R.J. (2015). Stem cells, progenitor cells, and lineage decisions in the ovary. Endocr Rev *36*, 65-91.

Ishihara, N., Nomura, M., Jofuku, A., Kato, H., Suzuki, S.O., Masuda, K., Otera, H., Nakanishi, Y., Nonaka, I., Goto, Y., et al. (2009). Mitochondrial fission factor Drp1 is essential for embryonic development and synapse formation in mice. Nat Cell Biol *11*, 958-966.

Jia, S., Ren, Z., Li, X., Zheng, Y., and Meng, A. (2008). smad2 and smad3 are required for mesendoderm induction by transforming growth factor-beta/nodal signals in zebrafish. J Biol Chem *283*, 2418-2426.

Kimura, T., Kaga, Y., Ohta, H., Odamoto, M., Sekita, Y., Li, K., Yamano, N., Fujikawa, K., Isotani, A., Sasaki, N., et al. (2014). Induction of primordial germ cell-like cells from mouse embryonic stem cells by ERK signal inhibition. Stem Cells *32*, 2668-2678.

Kobayashi, T., and Surani, M.A. (2018). On the origin of the human germline. Development *145*.

Liao, Y., Smyth, G.K., and Shi, W. (2014). featureCounts: an efficient general purpose program for assigning sequence reads to genomic features. Bioinformatics *30*, 923-930.

Ma, Q. (2013). Role of nrf2 in oxidative stress and toxicity. Annu Rev Pharmacol Toxicol *53*, 401-426.

Ma, S., Meng, Z., Chen, R., and Guan, K.L. (2019). The Hippo Pathway: Biology and Pathophysiology. Annu Rev Biochem *88*, 577-604.

Minhas, P.S., Latif-Hernandez, A., McReynolds, M.R., Durairaj, A.S., Wang, Q., Rubin, A., Joshi, A.U., He, J.Q., Gauba, E., Liu, L., et al. (2021). Restoring metabolism of myeloid cells reverses cognitive decline in ageing. Nature *590*, 122-128.

Narendra, D., Tanaka, A., Suen, D.F., and Youle, R.J. (2008). Parkin is recruited selectively to impaired mitochondria and promotes their autophagy. J Cell Biol *183*, 795-803.

Ohinata, Y., Ohta, H., Shigeta, M., Yamanaka, K., Wakayama, T., and Saitou, M. (2009). A signaling principle for the specification of the germ cell lineage in mice. Cell *137*, 571-584.

Peoples, J.N., Saraf, A., Ghazal, N., Pham, T.T., and Kwong, J.Q. (2019). Mitochondrial dysfunction and oxidative stress in heart disease. Exp Mol Med *51*, 1-13.

Picelli, S., Faridani, O.R., Bjorklund, A.K., Winberg, G., Sagasser, S., and Sandberg, R. (2014). Full-length RNA-seq from single cells using Smart-seq2. Nat Protoc *9*, 171-181.

Prigione, A., Fauler, B., Lurz, R., Lehrach, H., and Adjaye, J. (2010). The senescence-related mitochondrial/oxidative stress pathway is repressed in human induced pluripotent stem cells. Stem Cells *28*, 721-733.

Qin, X., Zhao, Y., Gong, J., Huang, W., Su, H., Yuan, F., Fang, K., Wang, D., Li, J., Zou, X., et al. (2019). Berberine Protects Glomerular Podocytes via Inhibiting Drp1-Mediated Mitochondrial Fission and Dysfunction. Theranostics *9*, 1698-1713.

Smith, A. (2017). Formative pluripotency: the executive phase in a developmental continuum. Development *144*, 365-373.

Tanaka, T., Urata, Y., Harada, M., Kunitomi, C., Kusamoto, A., Koike, H., Xu, Z., Sakaguchi, N., Tsuchida, C., Komura, A., et al. (2024). Cellular senescence of granulosa cells in the pathogenesis of polycystic ovary syndrome. Mol Hum Reprod *30*.

Tian, C., Heng, D., Zhao, N., Liu, L., Sheng, X., Chen, J., and Liu, L. (2023). Short telomeres impede germ cell specification by upregulating MAPK and TGFbeta signaling. Sci China Life Sci *66*, 324-339.

Tian, C., Liu, L., Ye, X., Fu, H., Sheng, X., Wang, L., Wang, H., Heng, D., and Liu, L. (2019a). Functional Oocytes Derived from Granulosa Cells. Cell Rep *29*, 4256-4267.

Tian, C., Liu, L., Ye, X., Fu, H., Sheng, X., Wang, L., Wang, H., Heng, D., and Liu, L. (2019b). Functional Oocytes Derived from Granulosa Cells. Cell Rep *29*, 4256-4267.e4259.

Tian, C., Liu, L., Ye, X., Fu, H., Sheng, X., Wang, L., Wang, H., Heng, D., and Liu, L. (2019c). Functional Oocytes Derived from Granulosa Cells. Cell Rep *29*, 4256-4267 e4259.

Tonelli, F., Iannello, L., Gustincich, S., Di Garbo, A., Pandolfini, L., and Cremisi, F. (2025). Dual inhibition of MAPK/ERK and BMP signaling induces entorhinal-like identity in mouse ESC-derived pallial progenitors. Stem Cell Reports *20*, 102387.

Varum, S., Rodrigues, A.S., Moura, M.B., Momcilovic, O., Easley, C.A.t., Ramalho-Santos, J., Van Houten, B., and Schatten, G. (2011). Energy metabolism in human pluripotent stem cells and their differentiated counterparts. PLoS One *6*, e20914.

Wahlestedt, M., Ameur, A., Moraghebi, R., Norddahl, G.L., Sten, G., Woods, N.B., and Bryder, D. (2014). Somatic cells with a heavy mitochondrial DNA mutational load render induced pluripotent stem cells with distinct differentiation defects. Stem Cells *32*, 1173-1182.

Yang, Q., Chen, W., Cong, L., Wang, M., Li, H., Wang, H., Luo, X., Zhu, J., Zeng, X., Zhu, Z., et al. (2024). NADase CD38 is a key determinant of ovarian aging. Nat Aging *4*, 110-128.

Ying, Q.L., Wray, J., Nichols, J., Batlle-Morera, L., Doble, B., Woodgett, J., Cohen, P., and Smith, A. (2008). The ground state of embryonic stem cell self-renewal. Nature *453*, 519-523.

Yu, S., Zhou, C., He, J., Yao, Z., Huang, X., Rong, B., Zhu, H., Wang, S., Chen, S., Wang, X., et al. (2022). BMP4 drives primed to naïve transition through PGC-like state. Nat Commun *13*, 2756.

Zhang, H., Jadhav, R.R., Cao, W., Goronzy, I.N., Zhao, T.V., Jin, J., Ohtsuki, S., Hu, Z., Morales, J., Greenleaf, W.J., et al. (2023). Aging-associated HELIOS deficiency in naive CD4(+) T cells alters chromatin remodeling and promotes effector cell responses. Nat Immunol *24*, 96-109.

Zhao, G., Dai, J., and Hu, Y. (2025). Development of regenerative therapies targeting fibrotic endometrium in intrauterine adhesion or thin endometrium to restore uterine function. Sci China Life Sci *68*, 2264-2276.

Zhao, Y., Zhao, T., Guan, J., Zhang, X., Fu, Y., Ye, J., Zhu, J., Meng, G., Ge, J., Yang, S., et al. (2015). A XEN-like State Bridges Somatic Cells to Pluripotency during Chemical Reprogramming. Cell *163*, 1678-1691.

Zhong, X., Cui, P., Cai, Y., Wang, L., He, X., Long, P., Lu, K., Yan, R., Zhang, Y., Pan, X., et al. (2019). Mitochondrial Dynamics Is Critical for the Full Pluripotency and Embryonic Developmental Potential of Pluripotent Stem Cells. Cell Metab *29*, 979-992 e974.

690 Zhou, C.J., Wang, X.Y., Dong, Y.H., Wang, D.H., Han, Z., Zhang, X.J., Sun, Q.Y., Carroll, J., and Liang, C.G.
691 (2022). CENP-F-dependent DRP1 function regulates APC/C activity during oocyte meiosis I. Nat
692 Commun *13*, 7732.
693 Zhou, W., Choi, M., Margineantu, D., Margaretha, L., Hesson, J., Cavanaugh, C., Blau, C.A., Horwitz,
694 M.S., Hockenbery, D., Ware, C., et al. (2012). HIF1α induced switch from bivalent to exclusively
695 glycolytic metabolism during ESC-to-EpiSC/hESC transition. Embo j *31*, 2103-2116.
696 Zhu, Z., Qin, S., Zhang, T., He, M., Zheng, W., Zhao, T., Gao, M., Chen, Z., Zhou, B., Xia, G., et al. (2023).
697 Pregranulosa cell-derived FGF23 protects oocytes from premature apoptosis during primordial follicle
698 formation by inhibiting p38 MAPK in mice. J Biol Chem *299*, 104776.
699 Zhu, Z., Xu, W., and Liu, L. (2022). Ovarian aging: mechanisms and intervention strategies. Med Rev
700 (2021) *2*, 590-610.
701

Figure 1. Mitochondrial function in granulosa cells.

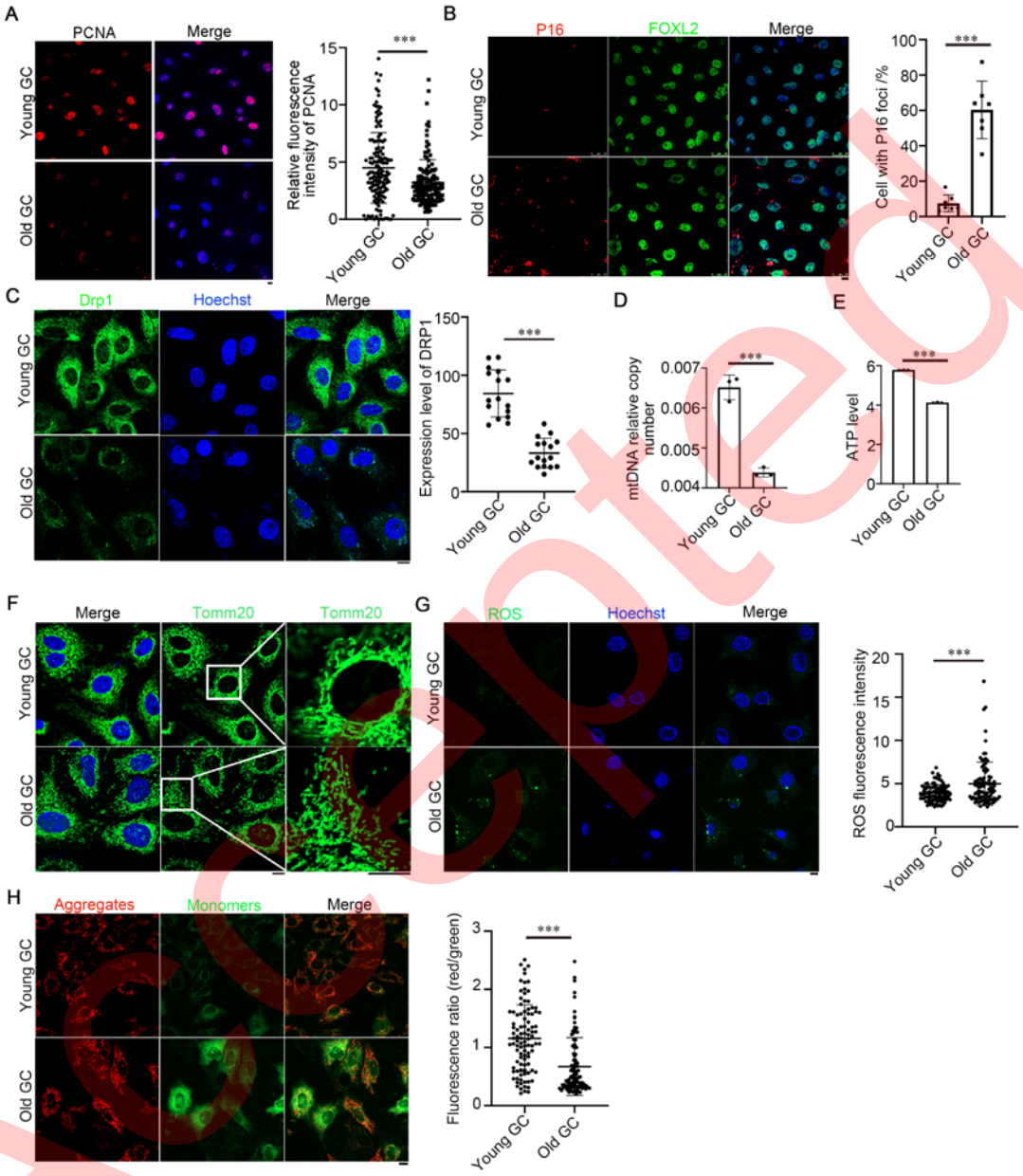

(A–C) Immunofluorescence staining of PCNA(A), P16(B), and DRP1(C) in granulosa cells (GCs), with fluorescence intensity quantification. Scale bar = 10 μm; ***P < 0.001. (D) Relative mtDNA copy numbers in GCs from young and reproductive-age mice. Data are presented as mean ± SD (n = 3); *** P < 0.001. (E) Analysis of ATP levels in GCs from young and aged mice. Data are expressed as mean ± SD (n = 3); *** P < 0.001. (F) Representative immunofluorescence images showing the expression of the mitochondrial marker Tomm20 in GCs from young (2 to 3-month-old) and aged (11 to 12-month-old) mice. Young GCs refer to GCs from young mice, and old GCs refer to GCs from old mice. Scale bar = 10 μm. (G) Detection of ROS levels in GCs using DCFH-DA, with fluorescence intensity quantification. Scale bar = 10 μm. Data are presented as mean ± SD; ***P < 0.001. (H) Representative images of the mitochondrial membrane potential as assessed using JC-1 dye. Scale bar = 10 μm. Scatter plot displaying the JC-1 aggregate/monomer fluorescence ratio. Data are presented as mean ± SD; ***P < 0.001.

Figure 2. Granulosa cells are reprogrammed to generate CiPSCs.

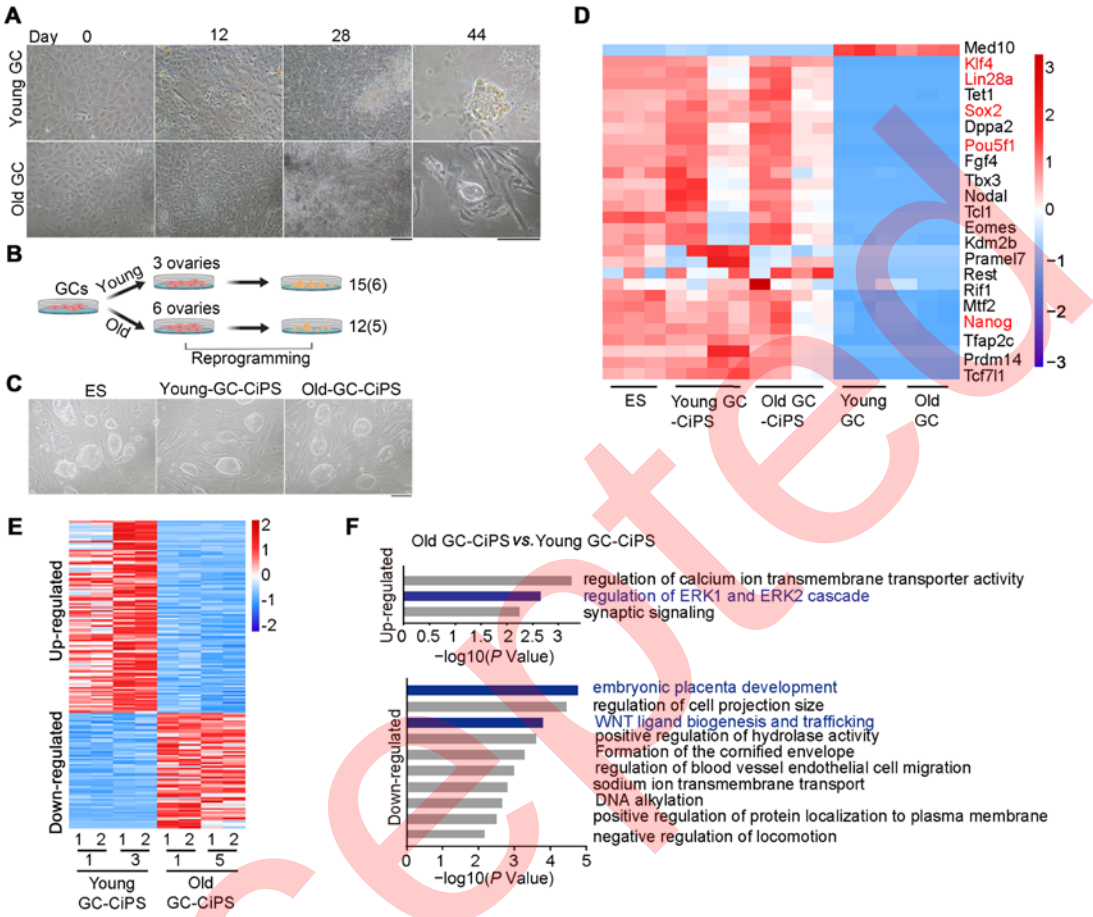

(A) Induction process of young GCs and old GCs into CiPSCs. Scale bar = 100 μm. (B) Overview of the induction process for generating CiPSCs from GCs using small molecule compounds. (C) Representative images of induced CiPSC lines derived from GCs. Scale bar = 100 μm. (D) Pluripotency-related genes that are differentially expressed in GCs, ESCs, young GC-CiPSCs, and old GC-CiPSCs. Red indicates upregulated gene expression (fold-change > 1.5, FDR < 0.05); blue indicates downregulated genes (fold-change > 1.5 and FDR < 0.05). (E) Differential gene expression analysis between young GC-CiPSCs and old GC-CiPSCs. Red indicates upregulated genes (fold-change > 1.5, FDR < 0.05); blue indicates downregulated genes (fold-change > 1.5 and FDR < 0.05). (F) Metascape enrichment analysis of signaling pathways related to genes upregulated and downregulated in young GC-CiPSCs and old GC-CiPSCs.

Figure 3. Old GC-CiPSCs exhibit decreased differentiation efficiency into PGCLCs.

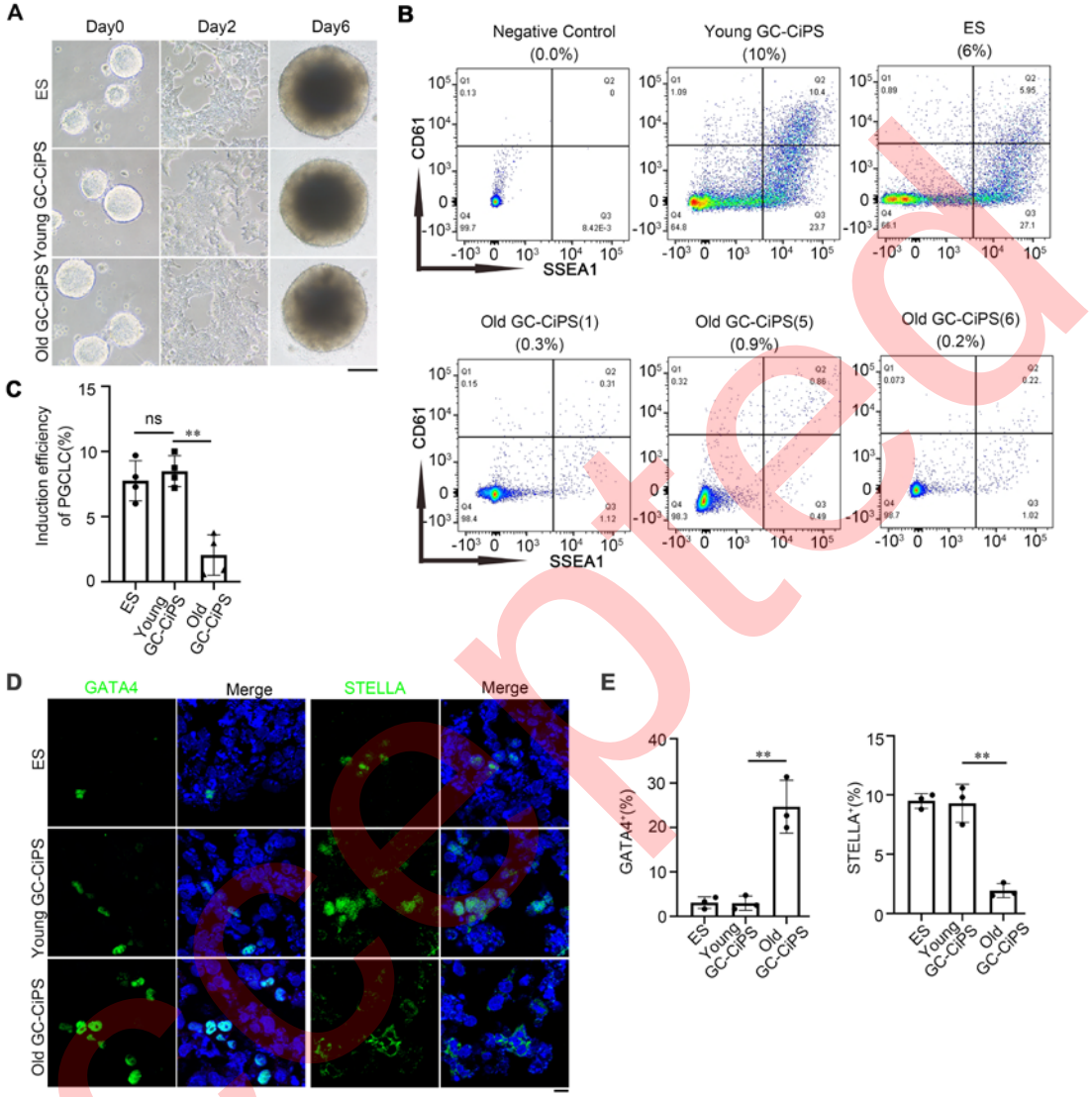

(A–C) Differentiation of ESCs, young GC-CiPSCs, and old GC-CiPSCs into PGCLCs, with corresponding statistical analysis (n =4); **P < 0.01, and ns indicates no significant difference. "Negative ctrl" is the negative control group, which lacked antibody treatment. (D) Representative immunofluorescence images showing the expression of GATA4 and STELLA in granulosa cells. Scale bar = 10 μm. (E) Quantification of GATA4 and STELLA fluorescence intensity; ***P < 0.001.

https://www.sciengine.com/doi/10.1007/s11427-025-3284-8

Figure 4. Mitochondrial function in CiPSCs.

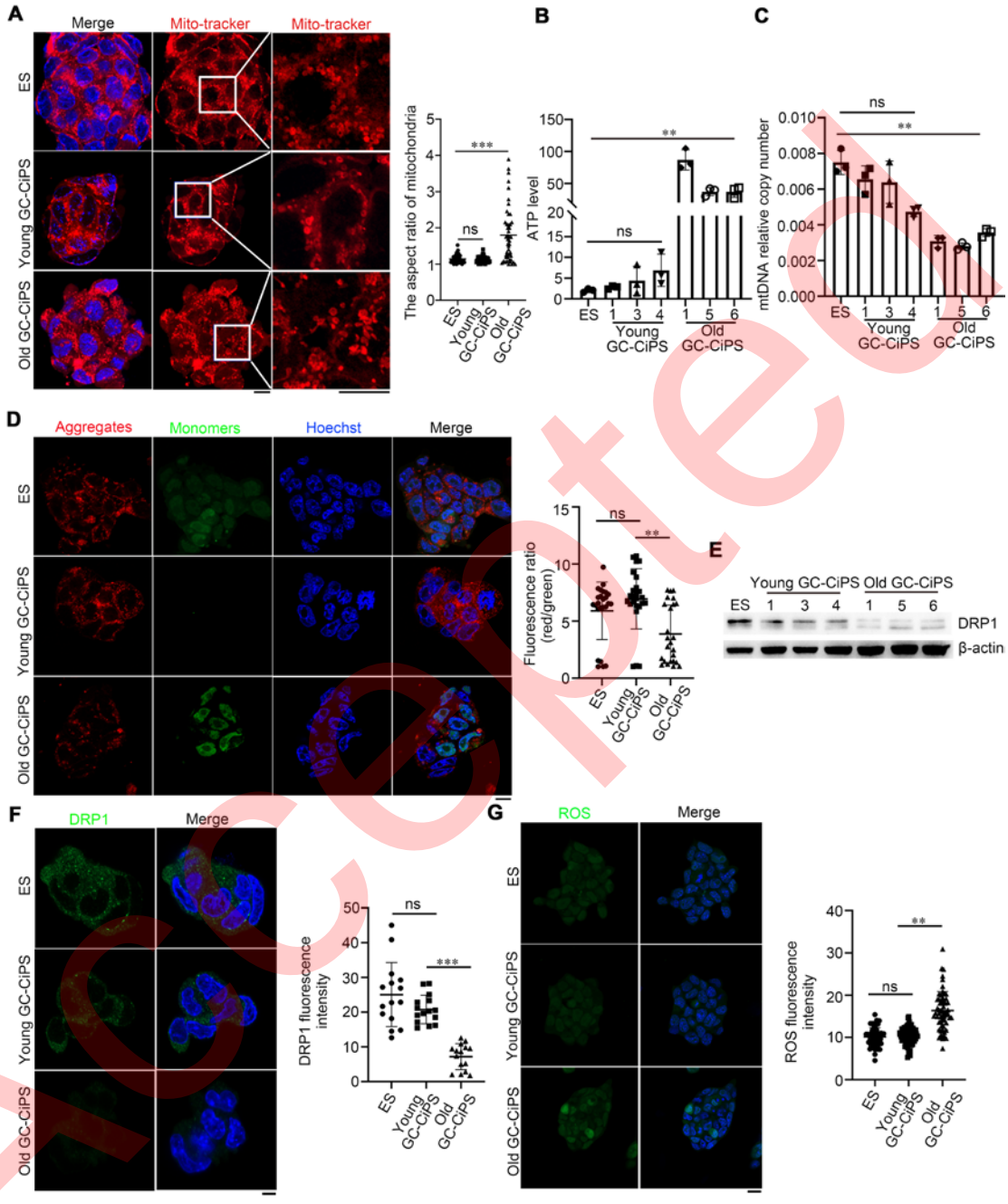

(A) Young and old CiPSCs were labeled with MitoTracker Red to visualize the morphology and localization of active mitochondria. (B) Quantitative analysis of relative ATP levels in young and old GCs, as well as in young and old CiPSCs. Data are presented as mean ± SD, n = 3 for each genotype. (C) Relative mtDNA copy number in ESCs and young and old CiPSCs. Data are presented as mean ± SD (n = 3); **P < 0.01. (D) Assessment of mitochondrial membrane potential in ESCs and young and old CiPSCs using JC-1 dye. Representative fluorescence images show JC-1 aggregates (red), monomers (green), Hoechst 33342 (blue, nuclei), and merged images. Quantitative analysis of the mitochondrial aspect ratio in ESCs and young and old GC-CiPSCs. Scale bar = 10 μm; ***P < 0.001. (E–F) Expression levels of DRP1 in ESCs and CiPSCs. (G) CiPSCs were labeled with DCFH-DA to visualize ROS levels. Scale bar = 10 μm.

https://www.sciengine.com/doi/10.1007/s11427-025-3284-8

Figure 5. MAPK/ERK pathway inhibition enhances the induction efficiency of old GC-CiPSCs into PGCLCs.

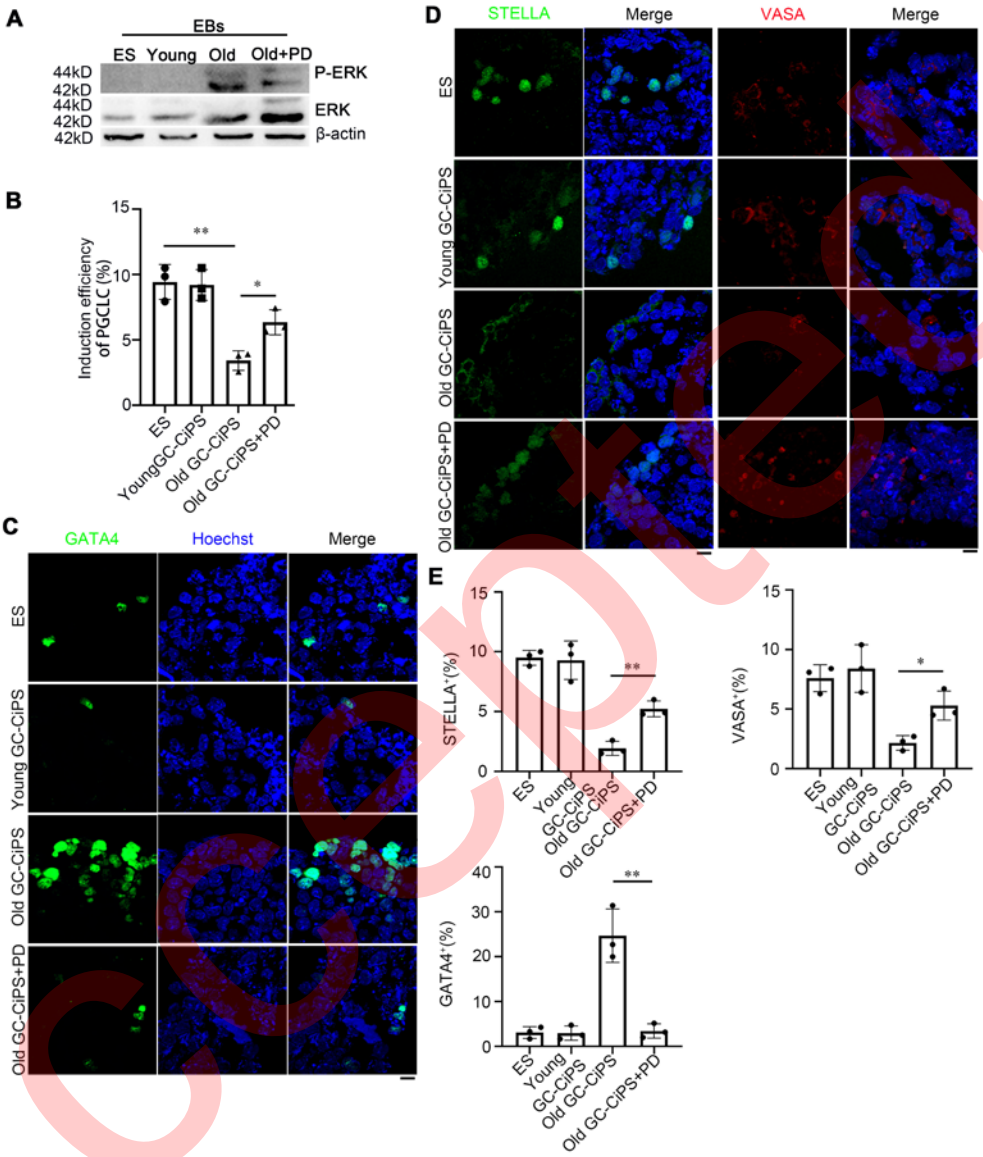

(A) Induction efficiencies of young GC-CiPSCs, old GC-CiPSCs, and old GC-CiPSCs treated with 1 μM PD0325901 to PGCLCs were measured (n = 3); **P < 0.01 and *P < 0.05. (B) Expression levels of P-ERK and ERK in EBs induced by old CiPSCs were assessed by western blot analysis. (C–D) Immunofluorescence staining for VASA, STELLA, and GATA4 in PGCLCs. Scale bar = 10 μm. (E) Quantification of the number of positive cells for STELLA, VASA, and GATA4 in young and old PGCLCs. Data are presented as mean ± SD; ***P < 0.001.

https://www.sciengine.com/doi/10.1007/s11427-025-3284-8

Figure 6. Changes in the gene expression of PGCLCs following MAPK/ERK signaling pathway inhibition.

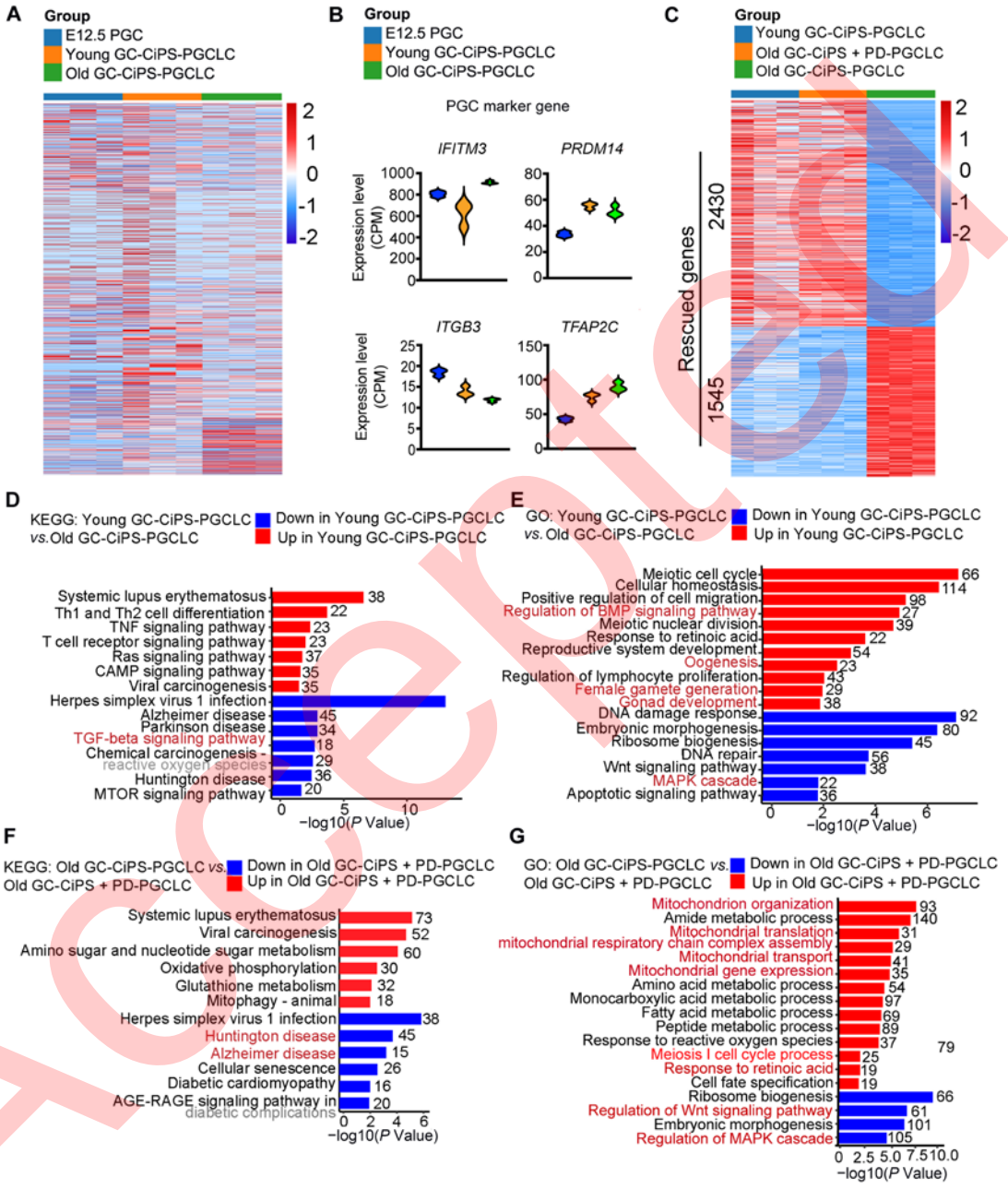

(A) Global gene expression heatmaps of PGCs, young GC-CiPS-PGCLCs, and old GC-CiPS-PGCLCs. (B) Diagrams illustrating the expression levels of characteristic germ cell marker genes in PGCs, young GC-CiPS-PGCLCs, and old GC-CiPS-PGCLCs. (C) Heatmap showing the effect of inhibiting the MAPK/ERK signaling pathway: 1,545 genes were reversed and inhibited, and 2,430 genes were reversed and activated (fold-change > 1.5, FDR < 0.05). (D, F) KEGG pathway analysis revealed the signaling pathways enriched in DEGs in PGCLCs (fold-change > 1.5, FDR < 0.05). (E, G) GO analysis revealed the biological processes enriched in DEGs in PGCLCs (fold-change > 1.5, FDR < 0.05).

Figure S1. Gene expression differences between young and old oocytes.

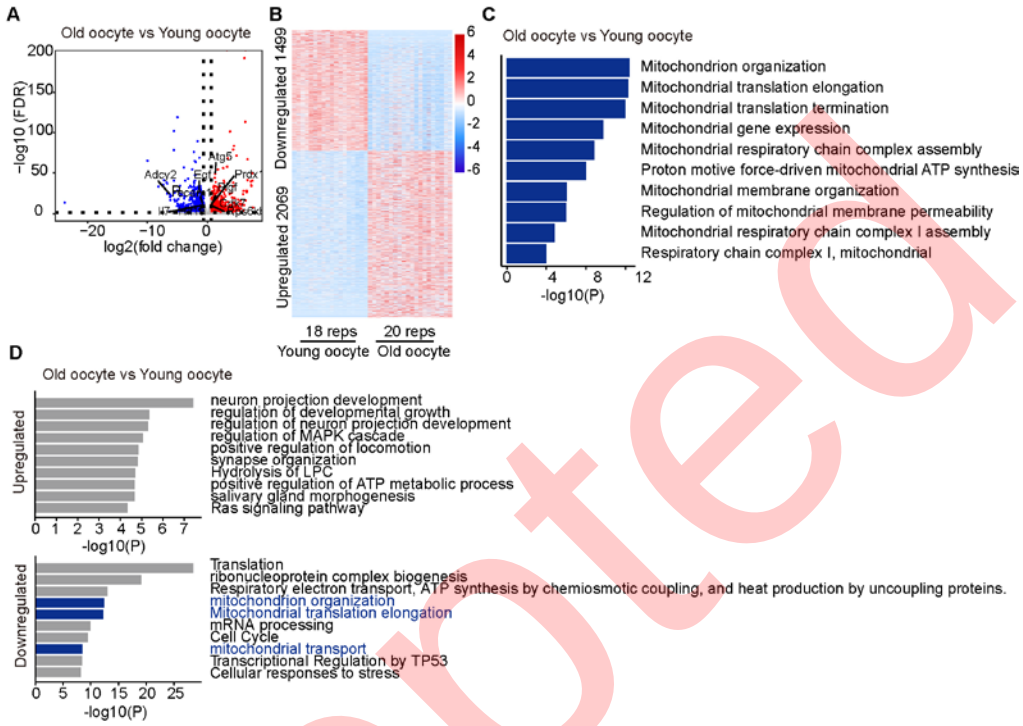

(A) Volcano plot illustrating the distribution of DEGs between young and old oocytes. Red dots represent upregulated genes (fold-change > 1.5 and FDR < 0.05). Blue dots indicate downregulated genes (fold-change > 1.5 and FDR < 0.05), and gray dots represent genes whose expression did not significantly change. (B) Differentially expressed genes between young and old oocytes. Red represents upregulated genes (fold-change > 1.5, FDR < 0.05), whereas blue indicates downregulated genes (fold-change > 1.5 and FDR < 0.05). (C) Histogram showing mitochondria-related pathways enriched in genes whose expression was downregulated in old oocytes. (D) Signaling pathways associated with the up- and downregulation of genes differentially expressed between young oocytes and old oocytes, as identified by Metascape.

Figure S2. Mitochondrial function in GV oocytes.

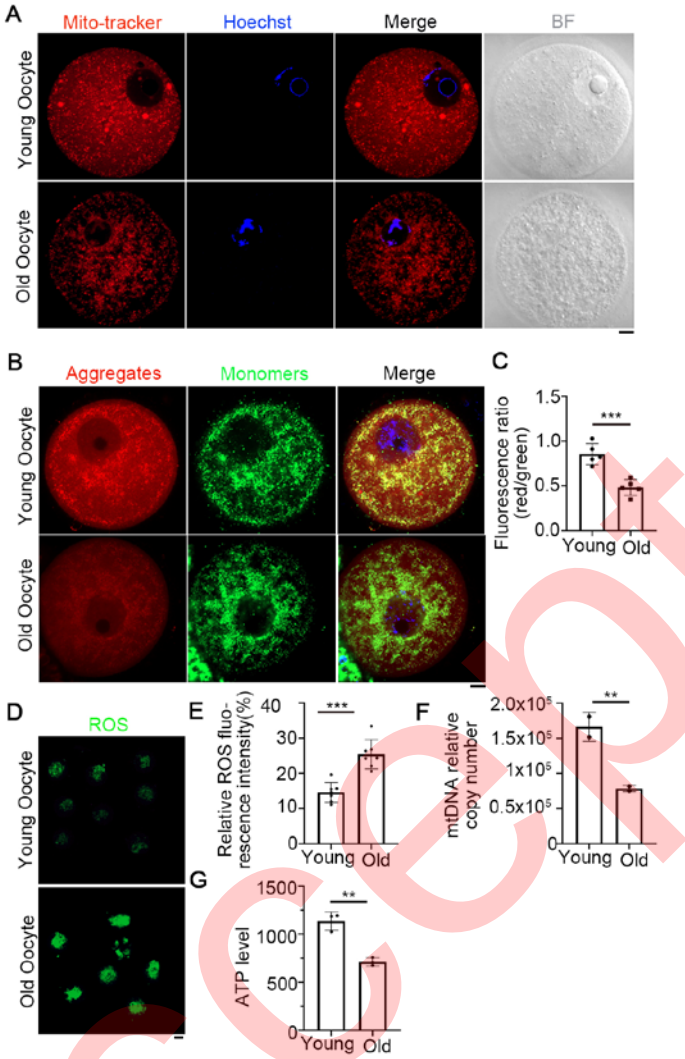

(A) Young and old GV oocytes were labeled with Mito-Tracker Red to visualize the localization of active mitochondria. "Young oocyte" refers to GV oocytes from young mice, and "old oocyte" refers to GV oocytes from old mice. Scale bar = 10 μm. (B) Assessment of mitochondrial membrane potential in young and old oocytes using JC-1 dye. Representative fluorescence images show JC-1 aggregates (red), monomers (green), and merged images. Scale bar = 10 μm. (C) Scatter plot showing the JC-1 aggregate/monomer fluorescence ratio. Data are presented as mean ± SD, n = 5; ***P < 0.001. (D) Young and old oocytes were labeled with DCFH-DA to visualize ROS levels. Scale bar = 10 μm. (E) Quantification of the fluorescence intensity of ROS in young and aged oocytes. Data are presented as mean ± SD; ***P < 0.001. (F) mtDNA copy number in young and old oocytes. Data are presented as mean ± SD, n = 10; **P < 0.01. (G) Quantitative analysis of relative ATP levels in young and old oocytes, n = 3; **P < 0.01.

Figure S3. Molecular characteristics of senescence in old granulosa cells.

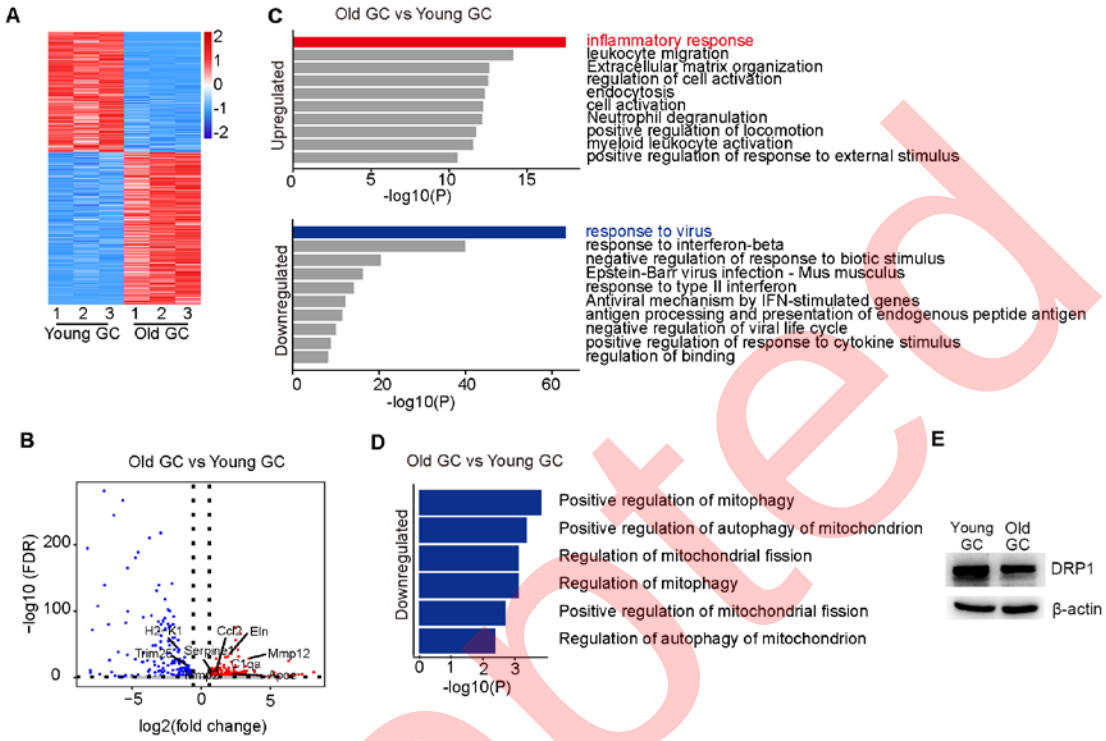

(A) Differentially expressed genes between young and old GCs. Red indicates upregulated genes (fold-change > 1.5, FDR < 0.05), and blue indicates downregulated genes (fold-change > 1.5 and FDR < 0.05). (B) Volcano plot showing the distribution of DEGs between young and old GCs. Red dots indicate upregulated genes (fold-change > 1.5 and FDR < 0.05), blue dots indicate downregulated genes (fold-change > 1.5 and FDR < 0.05), and gray dots indicate genes whose expression did not significantly change. (C) Up- and downregulated signaling pathways identified by Metascape analysis of differential gene enrichment between young and old GCs. (D) Histogram illustrating mitochondria-associated pathways enriched in downregulated genes in old GCs. (E) Western blot analysis showing reduced Drp1 protein levels in GCs from old mice compared with young mice.

Figure S4. Differences in gene expression among young GC-CiPSCs, old GC-CiPSCs, and ESCs.

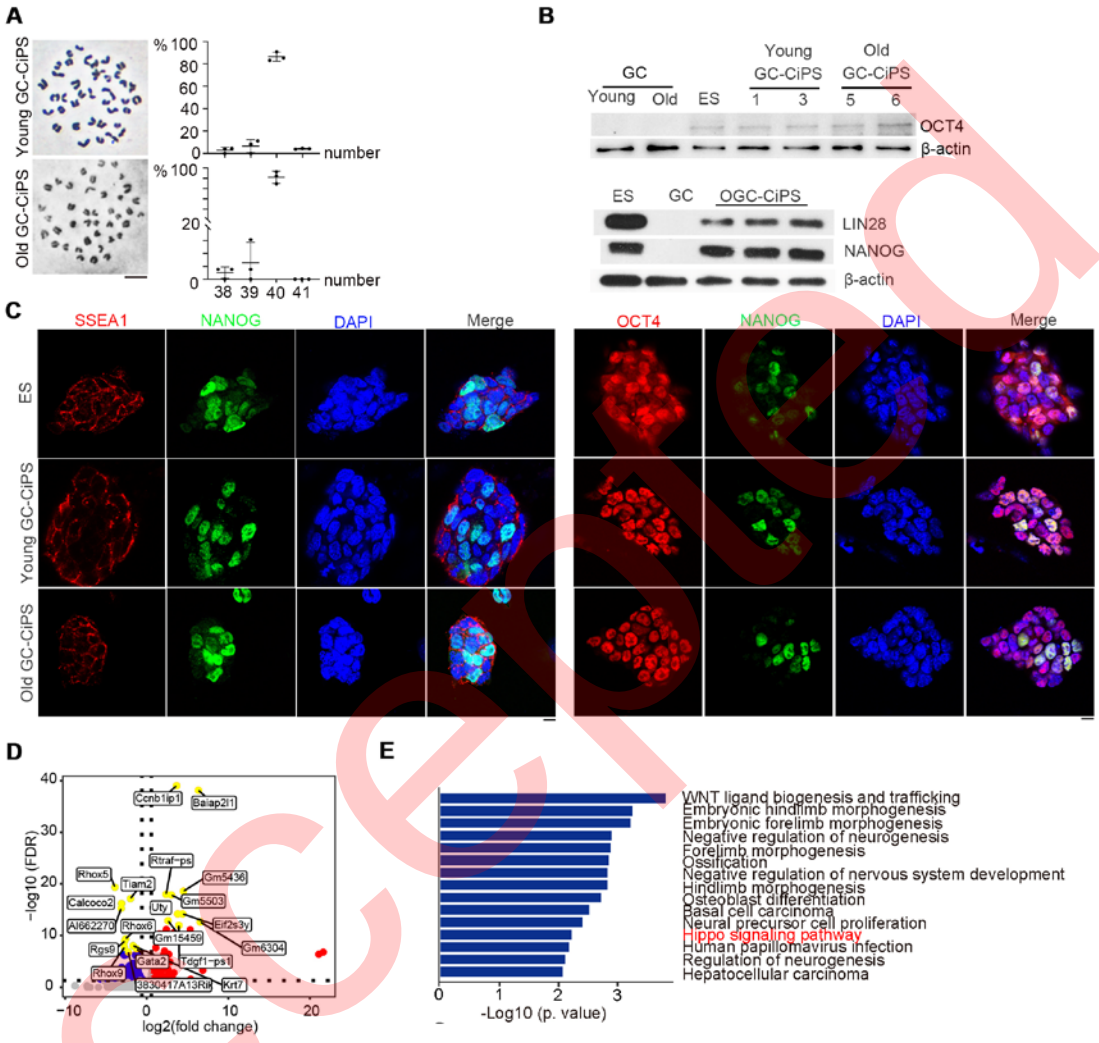

(A) Analysis of chromosome numbers in GC-CiPSCs. (B) Expression levels of the pluripotency markers OCT4, LIN28, and Nanog in ESCs and GC-CiPSCs. (C) Immunofluorescence staining of OCT4, NANOG, and SSEA1 in ESCs, young GC-CiPSCs, and old GC-CiPSCs, as observed by confocal microscopy. Scale bar = 10 μm. (D) Volcano plot showing the distribution of DEGs between young GC-CiPSCs and old GC-CiPSCs. Red dots indicate upregulated genes (fold-change > 1.5, FDR < 0.05), blue dots indicate downregulated genes (fold-change > 1.5, FDR < 0.05), and gray dots indicate genes whose expression did not significantly change. (E) Gene enrichment analysis of downregulated genes in old GC-CiPSCs, highlighting the Wnt ligand biogenesis and trafficking pathway.

Figure S5. Enhanced induction of PGCLCs by small molecules.

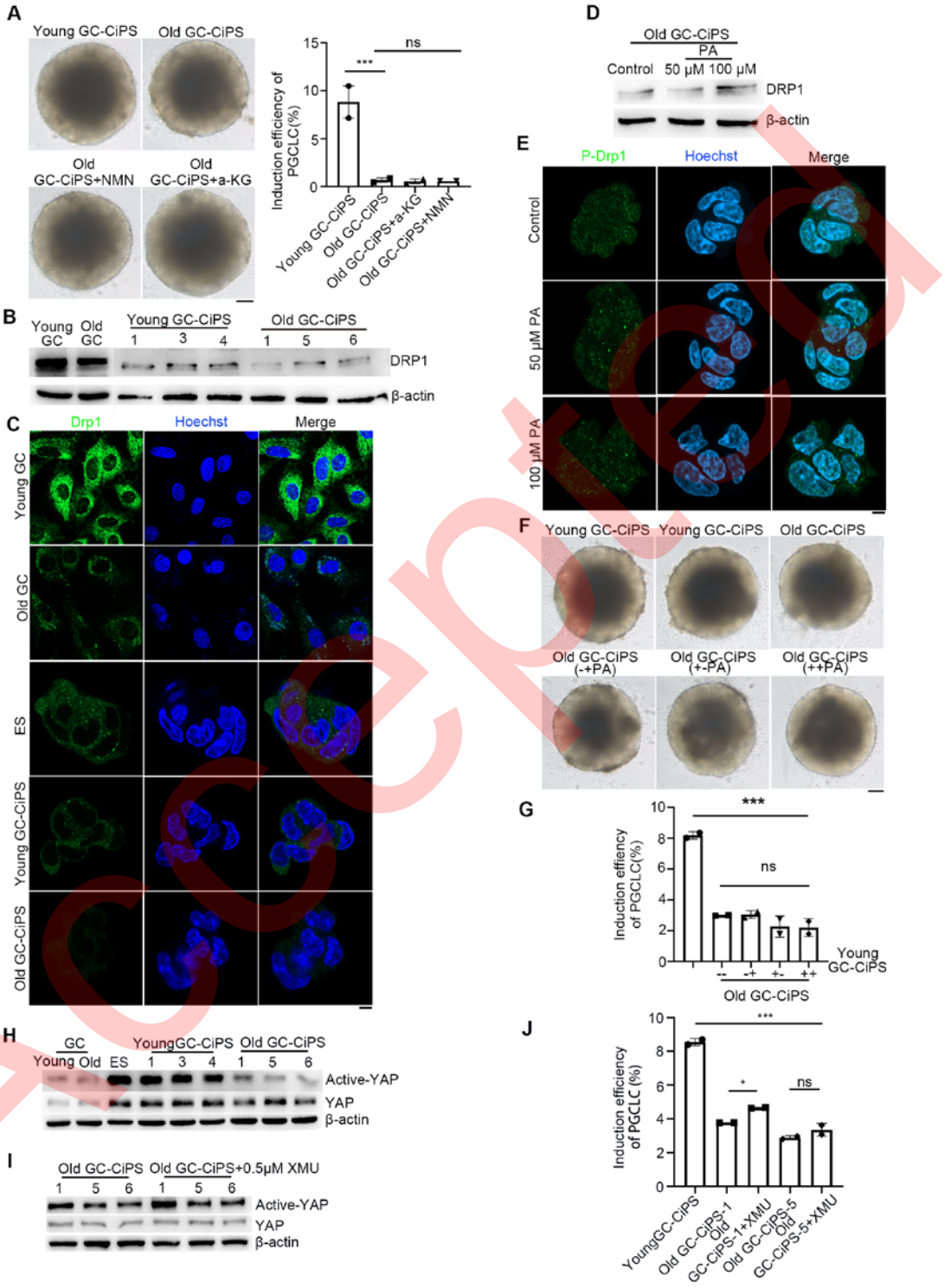

(A) Morphological structure and differentiation efficiency of old GC-CiPSCs into PGCLCs after treatment with NMN and α-KG. Scale bar = 100 μm. (B – C) Drp1 protein levels in the GCs of old mice were lower than those in the GCs of young mice, as shown by western blotting and immunofluorescence. (D–E) DRP1 expression in old GC-CiPSCs cultured with various palmitate concentrations for three generations. (F) Induction of PGCLCs from young GC-CiPSCs, old GC-CiPSCs, and old GC-CiPSCs + 100 μM palmitate observed under an optical microscope. Scale bar = 100 μm. (G) Induction efficiency of PGCLCs assessed by FACS. (H-I) Expression of

825 active YAP and YAP in GCs, ESCs, and GC-CiPSCs following XMU addition. (J) PGE2 induction
826 efficiency in the old group was assessed by FACS analysis after XMU treatment.

827 **Figure S6. Diagrams illustrating the expression levels of genes associated with**
828 **DNA methylation and histone acetylation in the transcriptomic data of young**
829 **and old GC-CiPSCs.**

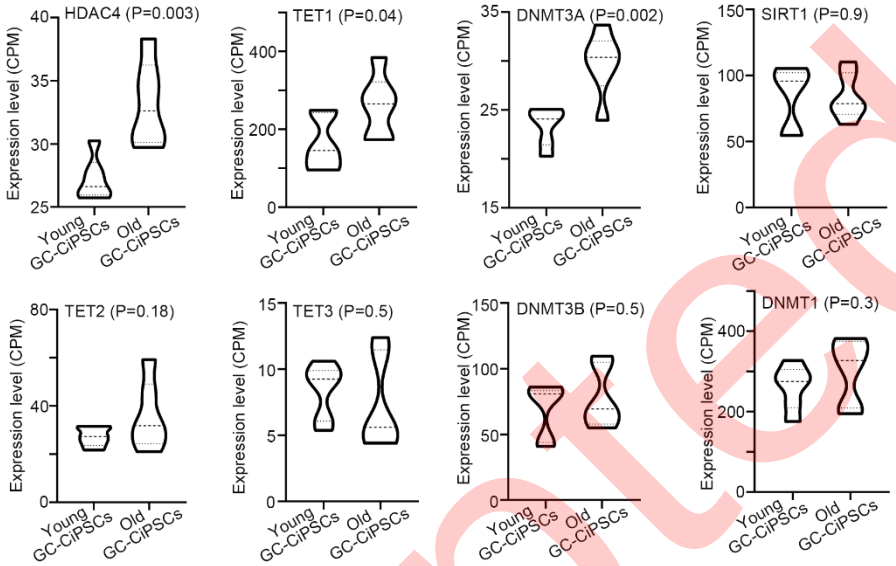

830
831